Cytoglobin-dependent NO-sGC-cGMP signaling regulates ventricular morphogenesis and diastolic function.

Adam Austin Clark[1], Rasmus Hejlesen[3], Tzu-Ting, Weng[1], Muddassar Iqbal[2], Akueba Bruce[2], Paola Corti[1#]

[1]Department of Biochemistry and Molecular Biology, University of Maryland School of Medicine, Baltimore, MD 21201

[2]Department of Medicine, University of Maryland School of Medicine, Baltimore, MD 21201

[3]MRC Human Genetics Unit, Institute of Genetics and Cancer, The University of Edinburgh, Edinburgh, EH4 2XU, UK

#Correspondence: Corti, Paola. Email: PCorti@som.umaryland.edu

Abstract

Aims. Hypoplastic left heart syndrome (HLHS) is a severe congenital heart disease characterized by ventricular hypoplasia and impaired cardiac function. Clinically, inhaled nitric oxide (NO) therapy is used to reduce pulmonary vascular resistance and improve cardiopulmonary stability in HLHS patients. However, whether NO signaling contributes to HLHS pathogenesis remains unknown. Cytoglobin (Cygb) is a heme-protein traditionally thought to limit NO bioavailability and downstream activation of the soluble guanylate cyclase (sGC) cyclic guanosine monophosphate (cGMP) signaling pathway. Unexpectedly, our recent work shows that Cygb enhances NO signaling through activation of NO synthase, leading to downstream activation of sGC-cGMP signaling. In zebrafish embryos, Cygb-dependent NO signaling is required for normal cilia motility and the establishment of correct cardiac laterality. Here, our aim was to determine whether Cygb-dependent NO-sGC signaling linked to cilia function regulates cardiac morphogenesis and contributes to ventricular hypoplasia in HLHS.

Methods and Results. We found that loss of *Cygb* (*cygb2*) in zebrafish disrupts NO-sGC signaling during cardiogenesis, altering cardiac progenitor organization and migration within the anterior lateral plate mesoderm. Disruption of these processes impairs heart tube morphogenesis, thereby producing a compact ventricle wall characterized by increased wall thickness (despite preserved cardiomyocyte number) reduced ventricle size and decreased stroke volume, recapitulating key features of HLHS. Genetic disruption of the sGC α-subunit (*gucy1a1)* and pharmacological NO scavenging phenocopy the *cygb2* mutant phenotype, resulting in reduced cGMP levels, compact ventricular architecture and decreased stroke volume. Consistently, restoration of NO-sGC signaling in *cygb2* mutants rescues early cardiac progenitor patterning, ventricular morphology and stroke volume.

Conclusions. These findings identify Cygb-dependent NO-sGC signaling as a critical developmental pathway for ventricular development and performance, temporally linking cardiac progenitor dynamics to cilia-dependent signaling associated with left-right patterning. This study further suggests that pharmacological activation of sGC may provide a therapeutic strategy for hypoplastic ventricular disease.

Keywords: Hypoplastic left heart syndrome, soluble guanylate cyclase, nitric oxide, cardiac development, zebrafish.

50 **Graphical Abstract**

51

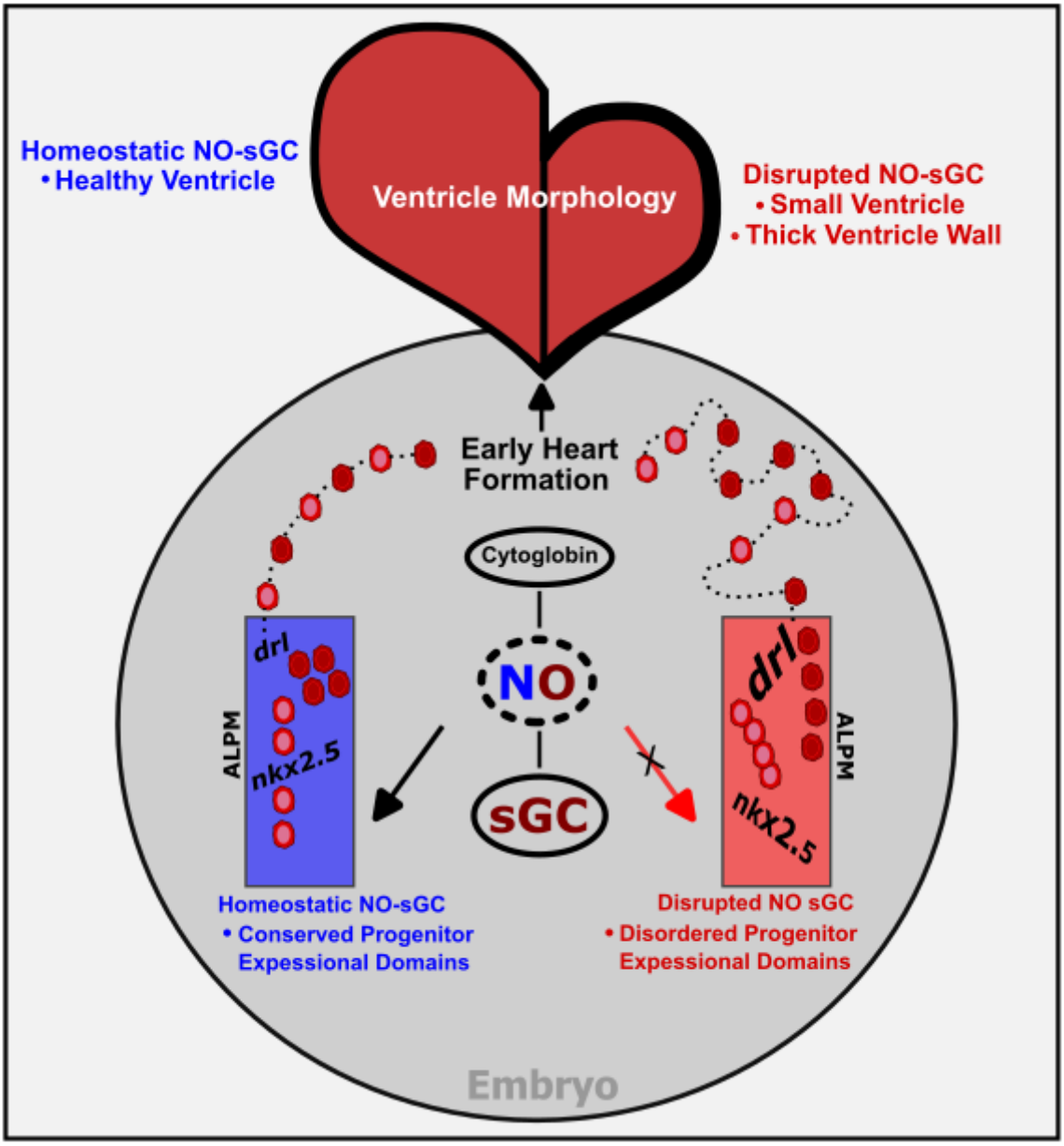

52

53

54

55

56

57

1. Introduction

Hypoplastic left heart syndrome (HLHS) is a complex congenital heart disease with a multigenic etiology.[1,2] Familial clustering supports a genetic basis, yet the majority of causative genes remain unidentified. The phenotype is heterogeneous, variably affecting the left ventricle, valves, and aortic outflow tract, and no single-gene mutation has been shown to reproduce the full HLHS spectrum in animal models. Traditionally, HLHS was attributed to diminished intracardiac flow during development, leading to secondary hypoplasia. However, recent work has shifted this paradigm, suggesting that HLHS may arise from primary defects in myocardial and endocardial development, resembling a developmental cardiomyopathy in origin rather than a purely hemodynamic lesion.[3] Additionally, an emerging body of evidence links HLHS to disturbances of left–right patterning and cilia function, suggesting a new developmental mechanism contributing to disease pathogenesis.[4] Based on case reports and large registry-based analyses,[4,5] HLHS has been observed in association with heterotaxy, situs inversus, gut malrotation, biliary atresia and splenic anomalies.[6-8] These observations further support the concept that defects in laterality determination and ventricular morphogenesis may share developmental origins. According to recent interpretations, HLHS may originate from early intrinsic disruptions in cardiac progenitors arising during and prior to heart tube formation,[9] and may occur in parallel with, or as a consequence of, abnormal left-right signaling. Findings from recessive forward genetic screens in fetal mice further support this view, revealing that cilia and cilia-transduced signaling pathways play central roles in HLHS pathogenesis.[10]

Integrative genetic analysis combining human sequencing with developmental datasets and mouse models of HLHS, identified CYGB as a candidate gene within a developmental gene network associated with the disease,[11] suggesting a potential role for CYGB in pathways regulating early cardiac morphogenesis. CYGB is a hexa-coordinate heme-containing globin expressed ubiquitously in vertebrate tissues.[12,13] Unlike its penta-coordinate relatives, hemoglobin and myoglobin, which primarily

83 bind and transport oxygen, CYGB is more prone to function as a redox-active enzyme regulating NO
84 metabolism through reversible redox cycling of its heme iron.[14] The reduced heme iron can catalyze
85 nitrite reduction to bioactive NO,[13,15] while the oxygenated heme iron can dioxygenate NO to inert
86 nitrate,[16-18] thus maintaining oxygen-dependent NO homeostasis. While these reactions are possible
87 in vitro, mouse studies indicate that the predominant physiological role of CYGB is to scavenge NO,
88 modulating vascular tone through NO deoxygenation[19] and to protect cells against oxidative stress via
89 superoxide dismutase-like activity.[20] Unexpectedly, we discovered a new critical role for Cygb in
90 development, where Cygb instead enhances NO signaling. The zebrafish *Cygb* (*cygb2)* knockout
91 exhibits cardiac laterality defects due to impaired NO signaling, a phenotype characteristic of human
92 disorders associated with defective cilia function. Mechanistically, we demonstrated that Cygb2
93 localizes to cilia within the zebrafish laterality organ (Kupffer's vesicle, KV), and increases NO
94 bioavailability through activation of the nitric oxide synthase enzyme (Nos2b).[21] Loss of *cygb2* disrupts
95 ciliary structure, motility and directional fluid flow, resulting in impaired KV activity and cardiac laterality
96 defects.[21] Whether this function is directly linked to cardiac morphogenesis mimicking HLHS remains
97 unknown and the extent to which Cygb-dependent regulation of laterality intersects, potentially through
98 ciliary mechanisms, has not been explored.
99
100 Zebrafish cardiac development initiates within the anterior lateral plate mesoderm (ALPM), where
101 bilateral populations of mesodermal progenitors undergo progressive spatial organization prior to overt
102 myocardial differentiation.[22,23] Between the 14–16 somite stages (ss), these progenitors undergo tightly
103 coordinated mediolateral convergence and anterior–posterior elongation to assemble a coherent
104 cardiac disc that subsequently develops into the linear heart tube.[23,24] At these stages of cardiac
105 development, ventricular formation is exquisitely sensitive to perturbations in progenitor number and
106 spatial positioning as even subtle defects in coordinated cell migration or tissue architecture can give
107 rise to abnormalities in ventricular morphogenesis, whereas atrial development may remain relatively

108 preserved due to its later progenitor contribution.[24,25] Importantly, these morphogenetic events critical
109 to ventricular development occur immediately downstream of KV mediated left–right axis
110 establishment,[23,26] raising the possibility that laterality patterning cues coordinating embryonic
111 asymmetry also influence spatial patterning and migratory behavior of cardiac progenitors, shaping
112 ventricular growth and chamber morphogenesis. One of the earliest markers of cardiac progenitors in
113 zebrafish is *draculin* (*drl*), a transcription factor activated during gastrulation that delineates bilateral
114 cardiac progenitor fields within the ALPM.[23,27] Alterations in ALPM spatial geometry, such as anterior–
115 posterior elongation of the *drl* domain, reflect early disruption of progenitor distribution or specification,[23]
116 defects expected to impair migratory cues and ventricle assembly. As development proceeds,
117 myocardial *drl* expression is restricted to first heart field-derived cardiomyocytes, providing a readout
118 of cardiac disc formation and heart tube assembly, stages that directly precede ventricular chamber
119 growth and functional maturation.[23]
120
121 *NKX2 homeobox 5* (*Nkx2.5)* encodes a conserved cardiac homeobox transcription factor expressed
122 within the forming cardiac disc at the transition from migratory cardiac progenitors to differentiated
123 myocardium.[23,27] In both mouse models and human patients, dysregulation of NKX2.5 activity is
124 associated with congenital heart diseases and hypoplastic ventricular phenotypes[28]. In the zebrafish
125 embryo, *nkx2.5* expression is conserved and is initially induced in bilateral ALPM domains as cardiac
126 progenitors converge toward the midline, coinciding with progenitor stabilization and the initiation of
127 chamber-specific transcriptional programs.[29] By 28 hpf, *nkx2.5* expression marks specified
128 cardiomyocytes within the heart tube, predominantly ventricular myocardium,[24] such that its expression
129 at this stage reflects proper myocardial differentiation and maintenance of cardiac identity.
130 While Cygb-dependent regulation of embryonic laterality is now established,[21] its role in coordinating
131 cardiac progenitor migration and myocardial differentiation remains unknown. Here, we demonstrate
132 that *cygb2* deficiency in zebrafish disrupts early cardiac progenitor organization and ventricular

133 chamber formation, producing a small, compact ventricle with reduced diastolic filling. These features
134 parallel ventricular hypoplasia and impaired diastolic function observed in HLHS. Crucially, these
135 defects are phenocopied in sGC mutants and fully rescued by pharmacological activation of NO-sGC
136 signaling, identifying a developmental pathway that links ciliary NO regulation to cardiac progenitor
137 morphogenesis and ventricular growth.
138

139 **2. Methods**

140 All animal studies were approved by the University of Maryland Institutional Animal Care and Use
141 Committee (IACUC-1022015), Baltimore, MD, USA. The programs and facilities are USDA registered
142 and covered under an assurance with the Office of Lab Animal Welfare (OLAW). Procedures followed
143 guidelines outlined by the NIH Guide for the Care and Use of Laboratory Animals (8th Edition, 2011).
144 Embryos were maintained at 28.5 °C until the desired developmental stage. Animals were euthanized
145 according to approved protocols; embryos >3 days post fertilization (dpf) to adult (anesthetic overdose
146 300mg/L buffered tricane), embryos <3dpf (paraformaldehyde immersion).
147

148 **2.1 Animal Studies**

149 For all experiments, clutch-matched embryos from dome stage (~ 4hpf) to 5dpf were randomly assigned
150 to treatment groups; sex cannot be determined at these stages. The AB (WT) genetic background was
151 used for generation of mutant and transgenic lines. Transgenic lines in this study include
152 Tg(*myl7:EGFP*) and Tg(*tbx5a:EGFP*; *tcf21:dsRED*). The *cygb2*^{801a} and the *gucy1a1*^{9bp} mutants were
153 generated using CRISPR-Cas9 genome editing as previously described[21] and guide RNAs are listed
154 in[21] and *Table S1*. Embryos were raised and screened for restriction enzyme site disruption (N1aIII)
155 using primers specific to exon 4 of *gucy1a1* (*Table S1*). The Tg(*myl7:EGFP*) and
156 Tg*(tbx5a:EGFP);*Tg*(tcf21:dsRED)* lines were crossed with *cygb2*^{801a} to produce
157 *cygb2*^{801a};Tg*(myl7:EGFP)*, *cygb2*^{801a};Tg*(tbx5a:EGFP);*Tg*(tcf21:dsRED),* and wildtype sibling lines.

158 **2.2 Stroke Volume**

159 Stroke volumes were calculated from live imaging. To calculate end-diastolic volume (EDV) and end-
160 systolic volume (ESV) frames were identified from high-speed wide-field (bright-field and fluorescent)
161 time-lapse videos of beating zebrafish hearts at the moments of maximal and minimal ventricular cavity
162 size. The long-axis length (*L*) and short-axis diameter (*D*) of the ventricle were measured from frames
163 using FIJI imaging software. EDV and ESV were calculated using the established prolate spheroid
164 model[30] according to the formula:

165 $V = \frac{\pi}{6} L D^2$

166 L represents ventricular long-axis length and D the diameter at mid-ventricle (*Figure S1*). Stroke volume
167 (SV) was derived as SV = EDV − ESV. Ventricle wall thickness was calculated at maximal and minimal
168 cavity size, identified from high-speed differential interference contrast (DIC) microscopy videos of
169 beating zebrafish hearts. The measurable area and length of the ventral-facing ventricle wall was
170 calculated using FIJI imaging software and the polygon selections and segmented line tool. The area
171 of the selected polygon was divided by the length of the measured wall to generate a ratio-based metric
172 of thickness. Bright field and fluorescent images were captured using a Zeiss Axio Observer inverted
173 microscope with attached Axiocam 807 mono camera and a Leica M165FC with attached K3C camera.

174

175 **2.3 Ventricle Volume and morphology**

176 Whole mount confocal z-series and compiled z-projections were collected on paraformaldehyde fixed
177 zebrafish embryos from 16ss to 3 days post fertilization. Immuno-labeled embryos were mounted on
178 glass slides and imaged on a Nikon Ti2 inverted W1 spinning disk confocal microscope with attached
179 Hamamatsu sCMOS camera. Collected z-series were compiled into max projections and 3D objects
180 with surface renderings using FIJI and Imaris imaging software. Ventricle volume and wall thickness
181 were calculated using thresholding on selected regions of interest (ROI). Z-slices covering full depth
182 and width of ventricle were compiled, and images were converted to 8-bit and set to grey scale. To

183 calculate the volume of myocardium, thresholding was set to black and white, area measurements for
184 signal-positive region were measured for each z-slice, summed, and multiplied by the distance between
185 z-slices. Ventricular lumen volume was calculated by measuring the area of signal-negative region
186 within the surrounding signal-positive region, summing the areas across z-slices and multiplying by z-
187 slice distance. To create a ratio-based metric to measure thickness across a 3-dimensional structure,
188 myocardium volume was divided by lumen volume. Cell density was calculated by dividing the total
189 cardiomyocyte number by the myocardium volume. Total ventricle cardiomyocyte number was
190 calculated using the collected z-series and FIJI imaging software. Z-slices spanning the full depth and
191 width of the ventricle were compiled, and analyzed frame by frame, and EGFP-positive cardiomyocytes
192 were marked, tracked, and counted. Ventricle volume at 5 dpf was generated from z-series collected
193 using a Zeiss LS7 Lighsheet confocal microscope. Ventricle area of z-slices was calculated by
194 thresholding (Huang Over Under) of the EGFP positive region within a ROI defining the ventricle
195 including the luminal space. Using FIJI and open-source macro code ventricular volume was calculated
196 by multiplying the summed areas by the distance between z-slices. Progenitor cell fusion, cardiac disc,
197 and heart tube areas were calculated using thresholding of EGFP and CY5 positive areas in selected
198 ROIs of max z-projections collected using spinning disk confocal microscopy.
199

200 **2.4 In situ hybridization**

201 Whole-mount in situ hybridization was performed on paraformaldehyde fixed zebrafish embryos as
202 previously described[21] at 10-12ss and 28 hpf using riboprobes targeting *drl*, *kinase insert domain*
203 *receptor like* (*kdrl*), and *nkx2.5*. Transcripts were amplified by PCR and cDNA was obtained from pooled
204 embryos using transcript specific primers (*Table S1*). Images were collected using bright-field
205 microscopy on a Zeiss Discovery V.8 SteReo stereoscope with attached Axiocam 503 color camera,
206 brightness and contrast were unaltered, and images were formatted using FIJI imaging software. To
207 determine expression patterning variance, raw counts of phenotype rankings were used for statistical

208 comparisons with the Fishers exact test, percentages were plotted for graphical representation, ns -
209 not significant ≥ 0.05, * P≤ 0.05, ** P≤ 0.01, *** P≤ 0.001, **** P≤ 0.0001.
210

211 **Drug Exposure**

212 Carboxy-PTIO potassium salt (2-4-carboxyphenyl-4,4,5,5-tetramethylimidazoline-1-oxyl-3-oxide;
213 cPTIO, Sigma–C221) and BAY 582667 (Cinaciguat, Bay58, Sigma–SML1532) were diluted in DMSO
214 and used at final concentrations of 500μM and 120μM respectively. (Z)-1-(N,N-diethylamino)diazen-1-
215 ium-1,2-diolate (DETA NONOate) (Cayman-82100) and (Z)-1-[N-(2-aminoethyl)-N-(2-
216 ammonioethyl)amino]diazen-1-ium-1,2-diolate (PAPA NONOate) (Cayman-2140) were resuspended
217 in sodium hydroxide and diluted in phosphate buffered saline at a final concentration of 250μM and
218 5.73μM. Drug exposure was achieved by incubation in embryo medium (E3).
219

220 **Immunohistochemistry**

221 Whole-mount immunohistochemistry was performed as previously described[21] using primary
222 antibodies for myosin heavy chain 6 (Developmental Studies Hybridoma Bank S46). Embryos were
223 mounted on glass slides with Vectashield Hardset Antifade Mounting Medium (H-1500-10) and imaged
224 on a Nikon Ti2 inverted W1 spinning disk confocal microscope equipped with an Hamamatsu sCMOS
225 camera.
226

227 **cGMP ELISA**

228 cGMP levels in zebrafish embryos were measured by competitive ELISA following manufactures
229 protocol (Enzo-ADI-900-164). Embryos at 28 hpf were incubated in 250μM DETA NONOate for 30
230 minutes at 28.5 °C. Fifty embryos per sample were pooled and homogenized in 0.1M hydrochloric acid
231 on ice. Lysates were centrifuged and the supernatant was collected for analysis. Samples were

232 assayed in triplicate at two dilutions. cGMP concentration was calculated based on interpolation to the
233 standard curve using a 95% confidence interval.
234
235 **Cell culture**
236 The human type II alveolar epithelial cell line A549 was kindly provided by Dr. Alan Cross (Professor,
237 Department of Microbiology and Immunology, University of Maryland School of Medicine). A549 cells
238 were cultured in RPMI-1640 media (Gibco-11875093) containing Penicillin/Streptomycin (Sigma-
239 P4333) and fungizone (Amphoterecin B, Gibco-15290-026), and 10% fetal bovine serum (FBS) (Sigma-
240 F4135) at 37^0 Celsius and 5% carbon dioxide. Cell cultures were passaged a minimum of three times
241 before performing experiments.
242
243 **Small interfering RNA**
244 Dicer Substrate RNA duplexed small interfering RNAs si-CYGB 13.1 and si-CYGB 13.2 targeting
245 human *CYGB* were selected using Integrated DNA Technologies "Predesigned DsiRNA Selection Tool".
246 DsiRNA-mediated gene silencing was validated through transfection of sub-confluent A549 monolayers
247 using Lipofectamine RNAiMAX transfection reagent (Thermo-13778030), non-targeting and human
248 *CYGB* targeting siRNAs for 48 hours. Si-CYGB 13.1 showed higher protein knockdown in Western Blot
249 experiments and was chosen for migration assays. To assess cell viability, transfected cells were
250 pelleted and resuspended in a 1:1 mixture of cell suspension and 0.4% Trypan Blue. Cells were counted
251 using a hemocytometer in a 0.05μm section. Cells excluding Trypan Blue were counted as live and
252 cells stained with Trypan Blue were counted as dead, viability was calculated as a percent of live cells
253 to total cell number.
254
255 **Western Blot**
256 A549 cells were lysed on ice in RIPA buffer (Sigma-R0278) containing protease inhibitor (Halt 1X,

257 Thermo-1860932). Lysates were centrifuged at 12,500 RPM for 20 min at 4°C. The BCA assay was
258 used to determine total protein concentration. Samples were loaded for gel electrophoresis in 4-20%
259 precast gels (Bio-Rad-4561094) using 100 µg total protein per sample. Following electrophoresis
260 protein was transferred to polyvinylidene fluoride membranes. Membranes were blocked with 3%
261 bovine serum albumin (BSA) for 2 hours at room temperature under gentle agitation. Membranes were
262 probed with primary rabbit anti-CYGB (Sigma-HPA017757) diluted at 1:1000 in 1% BSA and 0.1%
263 Triton X100 in phosphate buffer saline (PBST) overnight at 4^0 Celsius. Following 3 consecutive 5-
264 minute washes at room temperature in PBST membranes were probed with anti-Rabbit IgG-HRP
265 (Abcam-131366) at 1:10,000 in PBST with 1% BSA for 1 hour at room temperature. Following 3
266 consecutive 5-minute washes at room temperature in a solution of PBST protein bands were visualized
267 using Clarity Max Western ECL substrate (Bio-Rad-1705060) following manufacturer's protocol and a
268 Bio-Rad ChemiDoc MP imaging box. Following 3 consecutive 5-minute washes with PBST at room
269 temperature membranes were stripped using Restore Western Blot Stripping Buffer (Thermo-21059).
270 Blocking and probing procedure was repeated using primary rabbit anti-β-Actin antibody (Sigma-
271 A2066). Band intensity was normalized to β-Actin and quantified using FIJI imaging software.
272

273 **Wound healing assay**

274 A549 cells were seeded in 24-well plates at a density of 170,000 cells per well. After 24 hours cells
275 were transfected with 2.5pmol non-targeting DsiRNA, 1.25pmol and 2.5 pmol si-CYGB 13.1. At 48
276 hours post transfection, a scratch was introduced with a 10µl pipette tip. Following the scratch, cells
277 were washed with sterile 1x PBS and supplemented with RPMI-1640 media containing 10% (FBS).
278 Cultures were imaged at 0 and 24 hours post scratch on a Leica DM IL LED inverted microscope using
279 a 4X objective. Wound healing was assessed as percent migration into the scratch area relative to the
280 migration of control. Image analysis was conducted using FIJI imaging software.
281

282 **2.5 Statistical analysis**

283 Unless otherwise noted data are presented as mean ± SD, and statistical significance was determined
284 using an unpaired two-tailed *t*-test (or Mann–Whitney test for non-normal distributions), ns - not
285 significant ≥ 0.05, * P≤ 0.05, ** P≤ 0.01, *** P≤ 0.001, **** P≤ 0.0001.

286

287 **3. Results**

288 **Cytoglobin is required for ventricular development and cardiac function**

289 We previously defined a role for Cygb2 in cardiac laterality via regulation of cilia function. Here, we
290 investigated whether Cygb2 is required for cardiac morphogenesis and performance and whether these
291 are linked to laterality establishment. To visualize cardiac morphology, we generated a *cygb2* mutant
292 reporter line by crossing the previously characterized *cygb2*^{801a} mutant[21] with a transgenic reporter line
293 expressing EGFP under the control of the *myosin light chain 7* (*myl7)* promoter.[23] In zebrafish, *myl7*
294 expression begins at approximately the 16ss stage in cardiomyocyte progenitors regardless of eventual
295 chamber contribution to the atrium or ventricle.[23] We analyzed *myl7:EGFP* expression at 3 days post
296 fertilization (dpf), when cardiac morphology is established, and the ventricle and atrium exhibit
297 coordinated contraction and robust cardiac function. We first quantified the area of both cardiac
298 chambers and observed a significant decrease in the ventricle of *cygb2*^{801a} embryos compared to
299 wildtype controls, (*Figure 1A–C, Movies S1,2*), while atrial area remained unchanged (*Figure 1D*). To
300 precisely assess performance, we measured end diastolic volume (EDV) and end systolic volume
301 (ESV) from in vivo high-speed recordings and calculated stroke volumes (SV) using the prolate
302 spheroid method *(Figure S1).* Ventricles of *cygb2*^{801a} embryos showed a marked decrease in SV and
303 EDV with no change in ESV (*Figure 1E–H*), consistent with reduced diastolic filling rather than systolic
304 impairment. As *cygb2*^{801a} embryos exhibited cardiac laterality defects, we tested whether this
305 ventricular defect might arise secondarily from laterality disturbances. We compared embryos with
306 normal (situs solitus) and reversed (situs inversus) cardiac orientation within each genotype and

307 detected no differences in SV, *cygb2*^{801a} embryos displayed reduced SV relative to wildtype
308 independent of cardiac left-right orientation (*Figure S2A–F*). Assessment of SV at 5dpf revealed that
309 this phenotype persisted beyond initial ventricle morphogenesis (*Figure S3A–D, Movies S3-4*).
310 Additionally, ventricle volume was measured using light sheet confocal microscopy on fixed *myl7:EGFP*
311 samples and further supported the reduced ventricle volume observation and persistence at 5 dpf in
312 *cygb2*^{801a} compared to wildtype (*Figure S3E*). Collectively, these findings indicate a stable structural
313 hypoplasia rather than a transient developmental delay. Despite reduced chamber size, ventricular
314 cardiomyocyte number was unchanged (*Figure 1 I-J*). Instead, cells occupied a smaller volume, yielding
315 a more compact myocardium and a thicker ventricular wall (*Figure 1K–M*). These data indicate that
316 *cygb2* deficiency primarily affects ventricular morphogenesis and chamber remodeling, not
317 cardiomyocyte proliferation or survival. The reduced, thick-walled ventricle observed in *cygb2*^{801a}
318 embryos accompanied by reduced SV mirrors key structural features of HLHS thus *cygb2* deficiency
319 may represent a mechanistically relevant model of HLHS-like ventricular hypoplasia.
320

321 **Nitric oxide restores ventricular size and function in *cygb2* mutants.**

322 We previously showed that Cygb2 regulates cardiac laterality determination[21] through NO signaling. To
323 test whether the reduced SV in *cygb2*^{801a} embryos depends on NO, we first confirmed the acute
324 physiological action of NO donors. Ten-minute exposure at 78 hpf to the pharmacological NO donor
325 DETA-NONOate (DETA) increased SV in both wildtype and *cygb2*^{801a} embryos *(Figure S4A,B),*
326 consistent with the reported hemodynamic effect of NO in teleost fish larvae[31] where the increase in
327 SV results from reduced afterload due to relaxation of the outflow vasculature. A fast-releasing NO
328 donor, PAPA-NONOate (PAPA), produced a similar acute increase, validating the assay (*Figure*
329 *S4C,D*). To determine whether the altered ventricular developmental defects could be rescued by NO
330 supplementation, we tested the effect of chronic DETA treatment. DETA was administered in a vehicle
331 (sodium hydroxide), which alone did not affect SV (*Figure S4E*). We performed DETA treatments from

332 the 2ss stage to 3 dpf. Chronic exposure produced opposite outcomes depending on genotype, in
333 *cygb2*^{801a} embryos ventricular size increased with consequent rescue in SV, whereas in wildtype
334 embryos ventricular size was reduced, resulting in decreased SV (*Figure 2A,B*). Because prolonged
335 NO exposure affects cardiac morphogenesis rather than acute mechanics, these bidirectional
336 responses under identical dosing indicate that *cygb2* mutants possess a specific deficit in NO-
337 dependent developmental signaling, while excess NO in wildtype embryos disrupts the finely tuned
338 program governing ventricle morphogenesis. To provide further evidence supporting NO dependence,
339 we treated embryos at 2ss with the NO scavenger cPTIO to phenocopy the cardiac phenotype observed
340 in *cygb2* mutants (*Figure 2A,C*). As expected, ventricular volume was reduced by NO scavenging in
341 wildtype embryos and was further exacerbated in *cygb2*^{801a} embryos, consistent with a requirement for
342 NO signaling in normal ventricular development. A time course initiating DETA at stages from dome to
343 12ss showed maximal rescue when treatment began at dome stage to 2ss, diminishing by 12ss (*Figure*
344 *2D*), suggesting Cygb2-dependent NO signaling becomes critical for cardiac specification and
345 morphogenesis during early somitogenesis. Together, these findings demonstrate that *cygb2* is
346 required to maintain appropriate NO levels during early cardiac progenitor organization, thereby
347 ensuring proper ventricular morphogenesis and SV.
348
349 **Loss of Cygb2 disrupts early cardiomyocyte migration.**
350 Given that the ventricular phenotype observed in *cygb2*^{801a} embryos originates during early
351 development, we next examined cardiac morphogenesis to determine when these defects first emerge.
352 In zebrafish, cardiac progenitors originate bilaterally within the ALPM and progressively migrate toward
353 the midline, where they fuse to form the cardiac cone and subsequently the primitive heart tube. To
354 assess whether this process was altered in *cygb2* mutants, we analyzed the distribution of *myl7*-positive
355 cardiomyocyte precursors during heart field assembly. At 16ss when cardiomyocyte progenitors have
356 initiated migration but have not yet fused, *cygb2*^{801a} embryos displayed a significantly broader *myl7*-

357 positive domain compared with wildtype, indicating an expanded or delayed coalescence of cardiac
358 progenitors at this stage (*Figure 3A-C*). By 20ss, when the cardiac disc becomes morphologically visible
359 at the midline, the *myl7*-positive region remained wider and less compacted in *cygb2*^{801a} embryos,
360 occupying a larger total area relative to controls (*Figure 3D-F*). These results suggest that Cygb*2* is
361 required for the coordinated medial convergence of cardiomyocyte progenitors during heart field
362 assembly. As development progressed, the cardiac tube of *cygb2*^{801a} embryos remained visibly smaller
363 than in wildtype. At 34 and 48 hpf, the ventricular area was significantly reduced indicating that the
364 morphogenetic defect persists through the stages of heart tube elongation and chamber ballooning,
365 whereas the atrium appeared morphologically normal throughout (*Figure S5A-H).* This suggests a
366 ventricle-specific effect consistent with the smaller, compact ventricular morphology observed at later
367 stages. To establish NO as a critical regulator throughout ventricular morphogenesis, embryos were
368 treated with the NO donor DETA beginning at 2ss. These treatments restored *myl7*-positive cardiac
369 field at 16 and 20ss (*Figure 3A-F)* and rescued ventricular area at 34 and 48 hpf (*Figure S5A-H*) to near
370 wildtype levels. These findings demonstrate that *cygb2* is essential for the proper migration and
371 coalescence of cardiac progenitors and for subsequent expansion of the ventricular chamber, and that
372 both processes depend on NO-mediated signaling.

373 Upon observing aberrant organization of cardiac progenitors during midline convergence and cardiac
374 disc formation in *cygb2*^{801a} embryos, we directly tested whether cell migratory behavior was disrupted
375 using an in vitro wound-healing assay in the human type II alveolar epithelial A549 cell line. *CYGB*
376 transcript knockdown by small interfering RNA caused a dose-dependent reduction in cell migration
377 into the wound area (*Figure 3G,H*). CYGB protein knockdown efficiency and cell viability were
378 confirmed by Western Blot analysis (*Figure 3I,J and S6A*) and viability assay (*Figure S6B*). These data
379 suggest that abnormal cardiac progenitor contribution to early heart structures may result from
380 disruption of cellular machinery regulating cell migration and/or cell adhesion and further indicate that
381 Cygb-NO signaling influences migratory behavior across cell types and species.

382 **Soluble guanylate cyclase (sGC) is required for ventricle development and heart function.**
383 NO can signal through multiple mechanisms, including protein S-nitrosylation, nitration reactions and
384 formation of reactive nitrogen species. However, our data indicate that here NO primarily signals
385 through its canonical receptor sGC. Upon ligand binding, NO-sGC catalyzes the conversion of
386 guanosine triphosphate (GTP) to cGMP, thereby initiating secondary downstream signaling events[32].
387 To test whether the cardiac phenotype observed in *cygb2*^{801a} embryos depends on sGC, we generated
388 an sGC mutant (*gucy1a1*^{9bp}) using CRISPR/Cas9-mediated site-directed mutagenesis. Genomic DNA
389 from embryos derived from a maternal zygotic mutant line revealed a 9 bp deletion in exon 4 of the
390 sGCα1 subunit, which was confirmed at the genomic and mRNA level by Sanger Sequencing (*Figure*
391 *S7A*). Loss of the normal transcript was validated by in situ hybridization using a 300 bp probe spanning
392 the edited region, which showed markedly reduced hybridization signal in *gucy1a1*^{9bp} embryos
393 compared to wildtype, whereas a 1000 bp probe located downstream of the edited site produced
394 comparable staining in both mutants and wild type (*Figure S7B*). Functional loss of sGC activity in
395 *gucy1a1*^{9bp} embryos was confirmed by failure of DETA to restore cGMP levels in *gucy1a1*^{9bp} compared
396 to wildtype (*Figure S7E*). In contrast, DETA treatment restored cGMP levels in *cygb2*^{801a} embryos,[21]
397 supporting the interpretation that Cygb2 functions upstream of sGC to regulate NO-dependent cGMP
398 production during cardiac development. To determine whether sGC disruption phenocopies the
399 *cygb2*^{801a} cardiac defects observed here, we quantified ventricular performance in *gucy1a1*^{9bp} embryos
400 using DIC microscopy and high-speed imaging. SV was significantly reduced in *gucy1a1*^{9bp} compared
401 with wildtype embryos, driven by a decrease in EDV while ESV remained unchanged (*Figure 4A-E,*
402 *Movies S5,6*). This pattern mirrors the functional phenotype of *cygb2*^{801a} embryos, indicating that loss
403 of sGCα1 function recapitulates the diastolic filling defect observed in the *cygb2* mutant. Furthermore,
404 we tested SV at 5dpf in *gucy1a1* mutants and found that in both, reduced SV persisted at later
405 developmental stages (*Figure S7F-H, Movies S7,8*). To confirm that the observed phenotype reflects
406 disruption of a shared Cygb2-NO-sGC signaling pathway in both *cygb2*^{801a} *and gucy1a1*^{9bp} mutants, we

407 tested whether pharmacological activation of sGC in *cygb*^{801a} mutants could rescue cardiac function.
408 Treatment of *cygb*^{801a} mutants with the sGC activator Bay58 from 2ss to 34hpf fully restored SV (*Figure*
409 *4F-H),* confirming a critical role for sGC signaling in ventricular formation. Notably, neither DETA nor
410 Bay58 rescued stroke volume in *gucy1a1*^{9bp} mutants, as expected (*Figure S7C-D*). To assess a shared
411 phenotype of increased ventricle wall thickness, measurements were performed on live embryos at
412 3dpf. Wall thickness at diastole and systole was increased in *gucy1a1*^{9bp} (*Figure 4I-K, Movies S5,6*),
413 similar to that observed in *cygb2*^{801a} mutants (*Figure 4L-N, Movies S9,10*), indicating a conserved
414 phenotype across mutant models and analytic approaches. To further determine whether NO-sGC
415 signaling contributes to this phenotype, *cygb2*^{801a} mutants were treated from 2ss to 34hpf with DETA
416 and Bay58. These conditions fully restored ventricular wall thickness (*Figure 4L-N),* supporting a role
417 for Cygb-NO-sGC in ventricular morphogenesis.
418
419 **NO-sGC signaling regulates early cardiac progenitor organization.**
420 To determine whether Cygb2 and Gucy1a1 act through a shared molecular pathway during early
421 cardiogenesis, we analyzed key markers of the ALPM at 10–12ss, when early cardiac and endothelial
422 progenitors first emerge. In wildtype embryos, *drl* expression appeared as bilateral short, symmetrical
423 stripes flanking the midline, marking anterior mesoderm that gives rise to cardiac and vascular lineages.
424 In both *cygb2*^{801a} and *gucy1a1*^{9bp} embryos, *drl* domains were elongated, thinner, and extended
425 posteriorly, indicating disrupted convergence and defective compaction of the ALPM (*Figure 5A*).
426 Similarly, *kdrl*, which labels endothelial and endocardial progenitors, was expressed bilaterally in
427 compact domains close to the midline in wildtype embryos, but it was elongated, more widely
428 separated, and extended posteriorly in *cygb2*^{801a} and *gucy1a1*^{9bp} mutants (*Figure S8*). This finding is
429 consistent with delayed or uncoordinated migration of endothelial/endocardial precursors. Despite
430 these spatial changes, signal intensity was not diminished, suggesting that endothelial specification
431 may be largely preserved, while progenitor patterning appears shifted from anterior

432 (endothelial/endocardial) toward more posterior (hematopoietic) mesodermal domains. Expression of
433 the early cardiac transcription factor *nkx2.5* was also altered at 10-12ss. In wildtype embryos, *nkx2.5*
434 was expressed as two distinct, symmetrical domains within the ALPM, whereas in *cygb2*^{801a} and
435 *gucy1a1*^{9bp} mutants, expression was frequently asymmetric or spatially disorganized (*Figure 5B*),
436 suggesting loss of coordination between left and right cardiac fields. Importantly, wildtype siblings
437 generated during establishment of the maternal-zygotic *cygb2*^{801a} and *gucy1a1*^{9bp} lines were
438 outcrossed to minimize potential CRISPR off-target effects and displayed normal *drl*, *kdrl* and *nkx2.5*
439 expression patterns at all developmental stages examined (*Figure S9*). The *drl* expression patterning
440 abnormalities were rescued in *cygb2*^{801a} embryos treated with either DETA or Bay58 (*Figure 5A*),
441 confirming that early ALPM organization and synchronized cardiac specification depend on Cygb2-
442 mediated NO–sGC signaling. Additionally, *nkx2.5* expression was also partially normalized by DETA
443 treatment, although the strongest normalization was achieved in embryos treated with Bay58 (*Figure*
444 *5B*), confirming the importance of sGC signaling in this process. As *drl* marks early cardiac precursors
445 fields and *nkx2.5* labels a broader population encompassing later myocardial progenitors, this
446 differential rescue further supports the conclusion that NO–sGC signaling exerts its strongest influence
447 during the earliest stages of cardiac precursor organization and initial heart structure formation.
448

449 **NO–sGC signaling rescues ventricular gene expression.**

450 To assess whether early ALPM patterning defects persist during later stages of cardiogenesis, we
451 examined *drl*, and *nkx2.5* expression at 28 hpf, when the heart tube has formed and endothelial and
452 myocardial differentiation are underway. In wildtype embryos, *drl* expression is confined to the
453 developing vasculature and the endocardium; in contrast, *cygb2*^{801a} and *gucy1a1*^{9bp} embryos exhibited
454 reduced or absent *drl* expression in the heart tube (*Figure 6A*). This pattern is consistent with the shift
455 observed at earlier stages from anterior (endothelial/endocardial) toward more posterior
456 (hematopoietic) mesodermal domains. Consistently, *nkx2.5* expression in the ventricle was markedly

457 reduced in both *cygb2*^{801a} and *gucy1a1*^{9bp} embryos, indicating impaired myocardial contribution to this
458 region (*Figure 6B*). Treatment of *cygb2*^{801a} embryos with DETA or Bay58 restored *drl* and *nkx2.5*
459 expression patterns to near wildtype levels (*Figure 6A-B*). Together, these findings show that *cygb2*
460 and *gucy1a1* mutants share a common set of early and late ALPM abnormalities that can be corrected
461 by restoring NO-sGC signaling, linking early ALPM mis-patterning to the later emergence of a compact,
462 hypoplastic ventricle.
463

464 **4. Discussion**

465 Nitric oxide (NO) signaling is a central regulator of cardiovascular physiology, with established roles in
466 vascular tone, myocardial contractility, and hemodynamic homeostasis.[33-35] In contrast, the contribution
467 of NO signaling to early cardiac morphogenesis has been far less explored. Here, we show that Cygb2-
468 dependent NO–sGC signaling is required for ventricular formation during zebrafish heart development.
469 Loss of *cygb2* leads to a reduced SV associated with decreased ventricle volume, increased myocardial
470 wall thickness, elevated cellular density, and impaired diastolic filling. These defects arise from
471 abnormal migratory behavior of cardiac precursors, which display reduced migratory efficiency,
472 excessive cell-spreading, and subsequent hypercompaction within the forming heart tube. Importantly,
473 genetic loss of sGC (*gucy1a1*) fully phenocopies the *cygb2* mutant phenotype, and pharmacological
474 activation of NO-sGC signaling in *cygb2* mutants rescues ventricular volume, cardiac progenitor
475 migration, myocardial organization within the forming heart tube, and diastolic function. Together, these
476 data identify NO–sGC signaling downstream of Cygb2 as a central pathway coordinating myocardial
477 progenitor dynamics, ventricular morphogenesis, and functional maturation.

478 Cardiac progenitor migration is a fundamental driver of heart tube assembly and ventricular
479 morphogenesis and depends on tightly regulated cell polarity, adhesion turnover, and cytoskeletal
480 dynamics.[36-39] Disruption of these processes can profoundly alter chamber size and myocardial
481 architecture.[40,41] In this context, our data indicate that reduced NO–sGC signaling places cardiac

482 progenitors into a mechanically altered migratory state. NO-sGC-cGMP signaling is known to regulate
483 actomyosin contractility, focal adhesion turnover, and cortical tension across multiple cellular
484 contexts[42-44] and cytoglobin-dependent control of NO bioavailability represents a key upstream
485 determinant of this pathway[13,14]. Attenuation of NO–sGC signaling during development is therefore
486 predicted to stabilize cell–substrate and cell–cell adhesions, resulting in excessive cell spreading,
487 reduced migratory efficiency, and impaired cellular rearrangements at the tissue level. When such
488 mechanically altered cells enter the confined environment of the forming heart tube, increased adhesion
489 and cortical tension can bias morphogenesis toward tissue compaction and elevated cellular packing
490 as demonstrated in epithelial and mesenchymal morphogenetic models.[45,46] These properties provide
491 a mechanistic basis for the increased ventricular cell density observed in *cygb2* mutants, together with
492 the resulting thick-walled ventricle and impaired diastolic function.
493 We previously demonstrated that Cygb2 localizes to motile cilia and regulates cilia-dependent left–right
494 patterning through NO–sGC signaling during early zebrafish development,[21] establishing that Cygb2-
495 dependent NO–sGC signaling operates during early developmental windows critical for laterality
496 specification. The present study extends this role to ventricular formation while showing that ventricular
497 defects do not arise directly from altered left–right axis specification (*Figure S2*). However, ventricular
498 morphogenesis may still depend on cilia-associated signaling while remaining independent of final
499 laterality outcomes. Here, we found that pharmacological restoration of NO–sGC signaling rescues
500 ventricular morphology only when administered during early windows encompassing laterality
501 determination and early somitogenesis, whereas later treatment fails to restore ventricular size and
502 stroke volume, indicating that ventricular morphogenesis is temporally linked to early cilia-associated
503 signaling events. During this developmental window, we found that *drl* and *kdrl* expression is spatially
504 displaced and expanded within the ALPM, phenotypes consistent with defective cardiac progenitor
505 migration rather than primary loss of cardiogenic identity[36,38,39,41]. Notably, *nkx2.5*, normally expressed
506 symmetrically by early somitogenesis[47] is found asymmetric in *cygb2* mutants, suggesting altered

507 organization of subsets of cardiac progenitors. Recent single-cell studies indicate that *nkx2.5* marks
508 transcriptionally distinct progenitor populations within the ALPM[29] supporting the idea that the disrupted
509 signaling perturbs progenitor composition rather than uniformly impairing cardiac fate. Early migratory
510 defects likely lead secondarily to impaired differentiation or maintenance programs later, as reflected
511 by the reduction of *nkx2.5* and *drl* expression within ventricular territories at 28 hpf.[48,49] Importantly,
512 dysregulation of NKX2-5 is associated with several forms of congenital heart disease in humans,
513 including ventricular septal defects, tetralogy of Fallot, and HLHS, underscoring the relevance of these
514 findings to human cardiac pathogenesis.[47,50,51]

515 Sequencing studies have identified enrichment of rare variants in cilia and ciliopathy-associated genes
516 in subsets of HLHS patient cohorts,[4] supporting a framework in which cilia-dependent pathways
517 contribute to disease susceptibility in a subset of patients. Within this framework, zebrafish models
518 exhibiting reduced ventricular size with compact myocardium have emerged as informative systems for
519 studying cardiac morphogenesis and HLHS-like phenotypes.[9,49] In our *cygb2* mutant model, HLHS-like
520 ventricular hypoplasia originates from early events concomitant with cilia-dependent processes
521 involved in left-right patterning. Our data indicate two possible mechanistic pathways underlying this
522 phenotype. In one scenario, impaired NO-sGC signaling caused by loss of Cygb2 directly disrupts the
523 coordination of cardiac progenitor migration, regional specification, and ventricle expansion, leading to
524 reduced ventricular growth. In a second, distinct scenario, loss of Cygb2 perturbs cilia-dependent
525 processes that regulate early cardiac morphogenesis and myocardial growth, beyond their established
526 role in cardiac laterality, through downstream effects on progenitor deployment and tissue remodeling,[50]
527 independent of left–right axis determination. These mechanisms are not mutually exclusive and may
528 interact in the multigenic context of human HLHS, where combined defects in NO signaling and cilia-
529 associated pathways could converge on shared morphogenetic processes controlling ventricular
530 development. The *cygb2 and gucy1a1* models characterized here converge on the hallmark ventricular
531 phenotype of HLHS while revealing a distinct initiating axis centered on Cygb-dependent NO–sGC

532 signaling. Together with prior work demonstrating that modulation of NO bioavailability influences
533 myocardial plasticity and regeneration,[52] these findings establish NO–sGC signaling as a tractable
534 developmental pathway whose disruption leads to ventricular hypoplasia and whose restoration is
535 sufficient to rescue ventricular structure and function. Our data indicate that pharmacological activation
536 of sGC, previously unexplored in the context of hypoplastic ventricular disease, can restore ventricular
537 structure and function in HLHS-like phenotypes in vivo. These results position zebrafish as a valuable
538 model for interrogating early developmental mechanisms underlying ventricular hypoplasia and for
539 assessing sGC-targeted interventions in CHD.

540

541

542

543

544

545

546

547

548

549

550

551

552 **Author Contributions**

553 Adam Clark, Paola Corti designed and conducted experiments, analyzed data, and wrote the
554 manuscript. Paola Corti directed the research and conceptualization of experiments. Rasmus Hejlesen
555 and Muddassar Iqbal reviewed the manuscript. Rasmus Hejlesen constructed a data set for transcript
556 variance analysis that guided hypothesis generation. Weng Tzu-Ting conducted in situ hybridization
557 experiments. Muddassar Iqbal designed, conducted; and analyzed data for siRNA knockdown, wound
558 healing, and Western Blot experiments. Akueba Bruce conducted zebrafish husbandry and genotyping.

559

560 **Acknowledgements**

561 We are thankful to Dr. Mark T. Gladwin (Dean, University of Maryland School of Medicine) for expert
562 mentorship and guidance in project design. We thank Dr. Joseph Mauban, Dr. Shilpa Kumar and the
563 University of Maryland School of Medicine Center for Innovative Biomedical Resources, Confocal
564 Microscopy Core for invaluable assistance in imaging, and the Translational Genomics Lab for Sanger
565 Sequencing services.

566

567 **Conflict of Interest:** The authors declare no competing interests that influence the work reported in
568 this paper.

569

570 **Funding**

571 This work was supported by National Institutes of Health under awards number 5T32AR007592 and
572 R01HL168775.

573

574 **Data availability**

575 The data used to produce this article will be shared at reasonable request to the corresponding author.

576

577 **References**

578 1. Iascone M, Ciccone R, Galletti L, Marchetti D, Seddio F, Lincesso AR, Pezzoli L, Vetro A,
579 Barachetti D, Boni L, Federici D, Soto AM, Comas JV, Ferrazzi P, Zuffardi O. Identification of
580 de novo mutations and rare variants in hypoplastic left heart syndrome. *Clin Genet*
581 2012;**81**:542–554.
582 2. Yagi H, Liu X, Gabriel GC, Wu Y, Peterson K, Murray SA, Aronow BJ, Martin LJ, Benson DW, Lo
583 CW. The Genetic Landscape of Hypoplastic Left Heart Syndrome. *Pediatr Cardiol*
584 2018;**39**:1069–1081.
585 3. Grossfeld P, Nie S, Lin L, Wang L, Anderson RH. Hypoplastic Left Heart Syndrome: A New
586 Paradigm for an Old Disease? *J Cardiovasc Dev Dis* 2019;**6**.
587 4. Gabriel GC, Lo CW. Left-right patterning in congenital heart disease beyond heterotaxy. *Am J Med*
588 *Genet C Semin Med Genet* 2020;**184**:90–96.
589 5. Lin AE, Krikov S, Riehle-Colarusso T, Frias JL, Belmont J, Anderka M, Geva T, Getz KD, Botto LD,
590 National Birth Defects Prevention S. Laterality defects in the national birth defects prevention
591 study (1998-2007): birth prevalence and descriptive epidemiology. *Am J Med Genet A*
592 2014;**164A**:2581–2591.
593 6. Becker DJ, Islam S, Geiger JD. Biliary atresia associated with hypoplastic left heart syndrome: a
594 case report and review of the literature. *J Pediatr Surg* 2004;**39**:1411–1413.
595 7. Stankiewicz P, Sen P, Bhatt SS, Storer M, Xia Z, Bejjani BA, Ou Z, Wiszniewska J, Driscoll DJ,
596 Maisenbacher MK, Bolivar J, Bauer M, Zackai EH, McDonald-McGinn D, Nowaczyk MM,
597 Murray M, Hustead V, Mascotti K, Schultz R, Hallam L, McRae D, Nicholson AG, Newbury R,
598 Durham-O'Donnell J, Knight G, Kini U, Shaikh TH, Martin V, Tyreman M, Simonic I, Willatt L,
599 Paterson J, Mehta S, Rajan D, Fitzgerald T, Gribble S, Prigmore E, Patel A, Shaffer LG, Carter
600 NP, Cheung SW, Langston C, Shaw-Smith C. Genomic and genic deletions of the FOX gene

601 cluster on 16q24.1 and inactivating mutations of FOXF1 cause alveolar capillary dysplasia and
602 other malformations. *Am J Hum Genet* 2009;**84**:780–791.
603 8. Huseynova RA, Bin Mahmoud LA, Abdelrahim A, Alroiedy MA, Huseynov O. Polysplenia syndrome
604 with complex heart disease and jejunal atresia with malrotation in neonate: A case report. *Clin*
605 *Case Rep* 2020;**8**:848–851.
606 9. Huang M, Akerberg AA, Zhang X, Yoon H, Joshi S, Hallinan C, Nguyen C, Pu WT, Haigis MC,
607 Burns CG, Burns CE. Intrinsic myocardial defects underlie an Rbfox-deficient zebrafish model
608 of hypoplastic left heart syndrome. *Nat Commun* 2022;**13**:5877.
609 10. Yagi H, Lo CW. Left-Sided Heart Defects and Laterality Disturbance in Hypoplastic Left Heart
610 Syndrome. *J Cardiovasc Dev Dis* 2023;**10**.
611 11. Liu X, Yagi H, Saeed S, Bais AS, Gabriel GC, Chen Z, Peterson KA, Li Y, Schwartz MC,
612 Reynolds WT, Saydmohammed M, Gibbs B, Wu Y, Devine W, Chatterjee B, Klena NT, Kostka
613 D, de Mesy Bentley KL, Ganapathiraju MK, Dexheimer P, Leatherbury L, Khalifa O, Bhagat A,
614 Zahid M, Pu W, Watkins S, Grossfeld P, Murray SA, Porter GA, Jr., Tsang M, Martin LJ,
615 Benson DW, Aronow BJ, Lo CW. The complex genetics of hypoplastic left heart syndrome. *Nat*
616 *Genet* 2017;**49**:1152–1159.
617 12. Trent JT, 3rd, Hargrove MS. A ubiquitously expressed human hexacoordinate hemoglobin. *J Biol*
618 *Chem* 2002;**277**:19538–19545.
619 13. Corti P, Ieraci M, Tejero J. Characterization of zebrafish neuroglobin and cytoglobins 1 and 2:
620 Zebrafish cytoglobins provide insights into the transition from six-coordinate to five-coordinate
621 globins. *Nitric Oxide* 2016;**53**:22–34.
622 14. Amdahl MB, Sparacino-Watkins CE, Corti P, Gladwin MT, Tejero J. Efficient Reduction of
623 Vertebrate Cytoglobins by the Cytochrome b(5)/Cytochrome b(5) Reductase/NADH System.
624 *Biochemistry* 2017;**56**:3993–4004.

625 15. Reeder BJ, Ukeri J. Strong modulation of nitrite reductase activity of cytoglobin by disulfide bond
626 oxidation: Implications for nitric oxide homeostasis. *Nitric Oxide* 2018;**72**:16–23.
627 16. Halligan KE, Jourd'heuil FL, Jourd'heuil D. Cytoglobin is expressed in the vasculature and
628 regulates cell respiration and proliferation via nitric oxide dioxygenation. *J Biol Chem*
629 2009;**284**:8539–8547.
630 17. Gardner AM, Cook MR, Gardner PR. Nitric-oxide dioxygenase function of human cytoglobin with
631 cellular reductants and in rat hepatocytes. *J Biol Chem* 2010;**285**:23850–23857.
632 18. Tejero J, Shiva S, Gladwin MT. Sources of Vascular Nitric Oxide and Reactive Oxygen Species
633 and Their Regulation. *Physiol Rev* 2019;**99**:311–379.
634 19. Zweier JL, Ilangovan G. Regulation of Nitric Oxide Metabolism and Vascular Tone by Cytoglobin.
635 *Antioxid Redox Signal* 2020;**32**:1172–1187.
636 20. Zweier JL, Hemann C, Kundu T, Ewees MG, Khaleel SA, Samouilov A, Ilangovan G, El-Mahdy
637 MA. Cytoglobin has potent superoxide dismutase function. *Proc Natl Acad Sci U S A*
638 2021;**118**.
639 21. Rochon ER, Xue J, Mohammed MS, Smith C, Hay-Schmidt A, DeMartino AW, Clark A, Xu Q, Lo
640 CW, Tsang M, Tejero J, Gladwin MT, Corti P. Cytoglobin regulates NO-dependent cilia motility
641 and organ laterality during development. *Nat Commun* 2023;**14**:8333.
642 22. Yelon D. Cardiac patterning and morphogenesis in zebrafish. *Dev Dyn* 2001;**222**:552–563.
643 23. Kemmler CL, Riemslagh FW, Moran HR, Mosimann C. From Stripes to a Beating Heart: Early
644 Cardiac Development in Zebrafish. *J Cardiovasc Dev Dis* 2021;**8**.
645 24. Felker A, Prummel KD, Merks AM, Mickoleit M, Brombacher EC, Huisken J, Panakova D,
646 Mosimann C. Continuous addition of progenitors forms the cardiac ventricle in zebrafish. *Nat*
647 *Commun* 2018;**9**:2001.

648 25. Paffett-Lugassy N, Novikov N, Jeffrey S, Abrial M, Guner-Ataman B, Sakthivel S, Burns CE,
649 Burns CG. Unique developmental trajectories and genetic regulation of ventricular and outflow
650 tract progenitors in the zebrafish second heart field. *Development* 2017;**144**:4616–4624.
651 26. Hirokawa N, Tanaka Y, Okada Y. Left-right determination: involvement of molecular motor KIF3,
652 cilia, and nodal flow. *Cold Spring Harb Perspect Biol* 2009;**1**:a000802.
653 27. Mosimann C, Panakova D, Werdich AA, Musso G, Burger A, Lawson KL, Carr LA, Nevis KR,
654 Sabeh MK, Zhou Y, Davidson AJ, DiBiase A, Burns CE, Burns CG, MacRae CA, Zon LI.
655 Chamber identity programs drive early functional partitioning of the heart. *Nat Commun*
656 2015;**6**:8146.
657 28. Pashmforoush M, Lu JT, Chen H, Amand TS, Kondo R, Pradervand S, Evans SM, Clark B,
658 Feramisco JR, Giles W, Ho SY, Benson DW, Silberbach M, Shou W, Chien KR. Nkx2-5
659 pathways and congenital heart disease; loss of ventricular myocyte lineage specification leads
660 to progressive cardiomyopathy and complete heart block. *Cell* 2004;**117**:373–386.
661 29. Coskun H, Wang Y, Gao X, Chen K, Geoffrey Burns C, Burns CE. 3D spatial organization of
662 heterogeneous nkx2.5+ progenitors in the zebrafish heart field pre-patterns cardiovascular
663 development. *Nat Commun* 2025;**16**:11624.
664 30. Yalcin HC, Amindari A, Butcher JT, Althani A, Yacoub M. Heart function and hemodynamic
665 analysis for zebrafish embryos. *Dev Dyn* 2017;**246**:868–880.
666 31. Fritsche R, Schwerte T, Pelster B. Nitric oxide and vascular reactivity in developing zebrafish,
667 Danio rerio. *Am J Physiol Regul Integr Comp Physiol* 2000;**279**:R2200–2207.
668 32. Arnold WP, Mittal CK, Katsuki S, Murad F. Nitric oxide activates guanylate cyclase and increases
669 guanosine 3':5'-cyclic monophosphate levels in various tissue preparations. *Proc Natl Acad Sci*
670 *U S A* 1977;**74**:3203–3207.
671 33. Ignarro LJ. Nitric Oxide: A Unique Endogenous Signaling Molecule in Vascular Biology (Nobel
672 Lecture). *Angew Chem Int Ed Engl* 1999;**38**:1882–1892.

673 34. Gladwin MT. Deconstructing endothelial dysfunction: soluble guanylyl cyclase oxidation and the
674 NO resistance syndrome. *J Clin Invest* 2006;**116**:2330–2332.
675 35. Forstermann U, Sessa WC. Nitric oxide synthases: regulation and function. *Eur Heart J*
676 2012;**33**:829–837, 837a–837d.
677 36. Stainier DY. Zebrafish genetics and vertebrate heart formation. *Nat Rev Genet* 2001;**2**:39–48.
678 37. Buckingham SD, Ali DW. Computer simulations of high-pass filtering in zebrafish larval muscle
679 fibres. *J Exp Biol* 2005;**208**:3055–3063.
680 38. Abu-Issa R, Kirby ML. Heart field: from mesoderm to heart tube. *Annu Rev Cell Dev Biol*
681 2007;**23**:45–68.
682 39. Bakkers J. Zebrafish as a model to study cardiac development and human cardiac disease.
683 *Cardiovasc Res* 2011;**91**:279–288.
684 40. Hutson MR, Kirby ML. Model systems for the study of heart development and disease. Cardiac
685 neural crest and conotruncal malformations. *Semin Cell Dev Biol* 2007;**18**:101–110.
686 41. Vincent SD, Buckingham ME. How to make a heart: the origin and regulation of cardiac progenitor
687 cells. *Curr Top Dev Biol* 2010;**90**:1–41.
688 42. Surks HK, Mochizuki N, Kasai Y, Georgescu SP, Tang KM, Ito M, Lincoln TM, Mendelsohn ME.
689 Regulation of myosin phosphatase by a specific interaction with cGMP- dependent protein
690 kinase Ialpha. *Science* 1999;**286**:1583–1587.
691 43. Schlossmann J, Hofmann F. cGMP-dependent protein kinases in drug discovery. *Drug Discov*
692 *Today* 2005;**10**:627–634.
693 44. Prysyazhna O, Rudyk O, Eaton P. Single atom substitution in mouse protein kinase G eliminates
694 oxidant sensing to cause hypertension. *Nat Med* 2012;**18**:286–290.
695 45. Lecuit T, Lenne PF. Cell surface mechanics and the control of cell shape, tissue patterns and
696 morphogenesis. *Nat Rev Mol Cell Biol* 2007;**8**:633–644.

697 46. Heisenberg CP, Bellaiche Y. Forces in tissue morphogenesis and patterning. *Cell* 2013;**153**:948–
698 962.
699 47. Sultana N, Nag K, Hoshijima K, Laird DW, Kawakami A, Hirose S. Zebrafish early cardiac
700 connexin, Cx36.7/Ecx, regulates myofibril orientation and heart morphogenesis by establishing
701 Nkx2.5 expression. *Proc Natl Acad Sci U S A* 2008;**105**:4763–4768.
702 48. Moorman AF, Christoffels VM. Cardiac chamber formation: development, genes, and evolution.
703 *Physiol Rev* 2003;**83**:1223–1267.
704 49. Liu J, Stainier DY. Zebrafish in the study of early cardiac development. *Circ Res* 2012;**110**:870–
705 874.
706 50. Sutherland MJ, Ware SM. Disorders of left-right asymmetry: heterotaxy and situs inversus. *Am J*
707 *Med Genet C Semin Med Genet* 2009;**151C**:307–317.
708 51. George V, Colombo S, Targoff KL. An early requirement for nkx2.5 ensures the first and second
709 heart field ventricular identity and cardiac function into adulthood. *Dev Biol* 2015;**400**:10–22.
710 52. Rochon ER, Missinato MA, Xue J, Tejero J, Tsang M, Gladwin MT, Corti P. Nitrite Improves Heart
711 Regeneration in Zebrafish. *Antioxid Redox Signal* 2020;**32**:363–377.
712
713
714
715
716
717
718
719
720
721

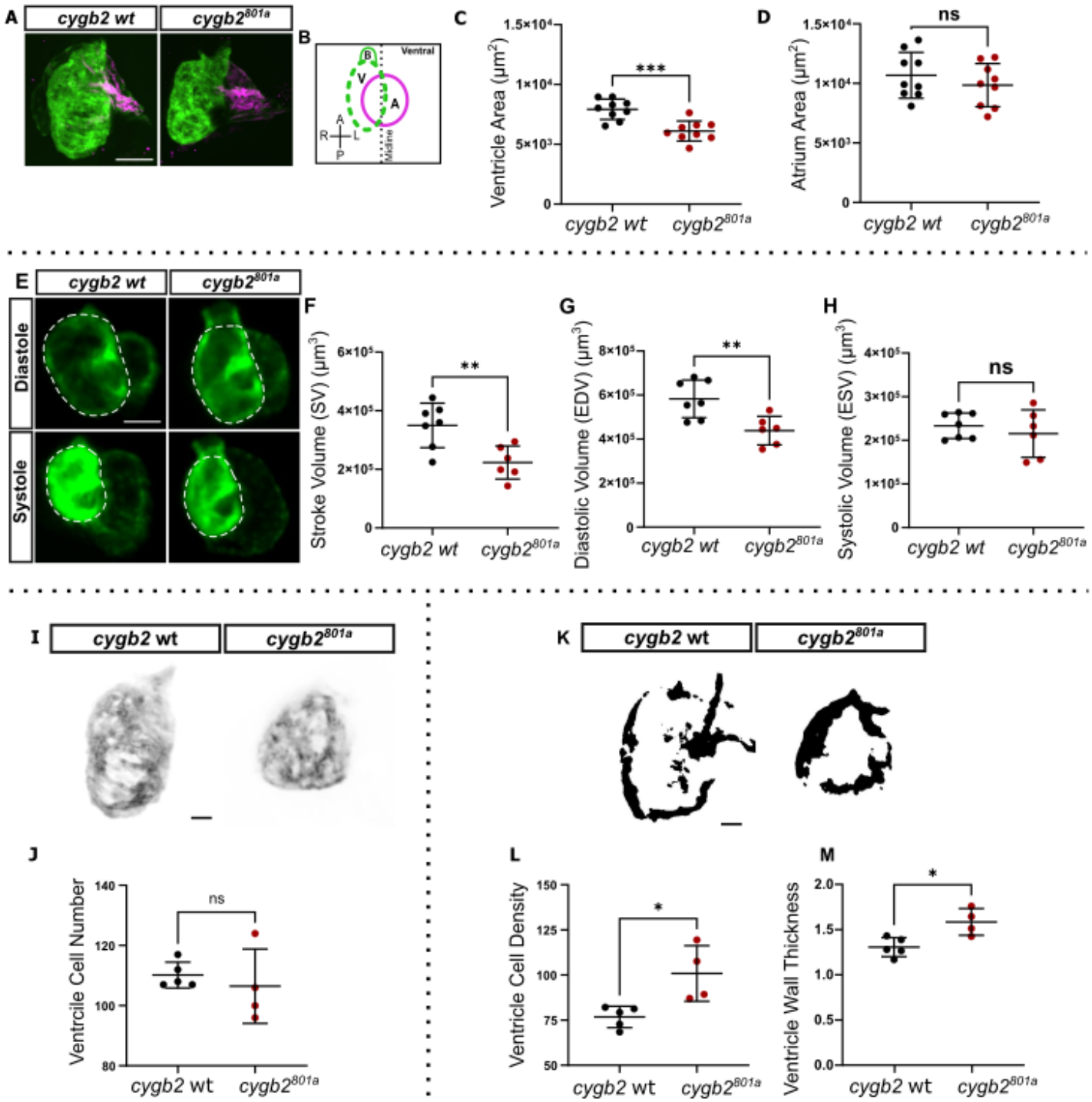
A
cygb2 wt
cygb2801a
B
Ventral
B
V
A
A
R
L
P
Midline
C
Ventricle Area (μm2)
1.5×104
1×104
5×103
0
***
cygb2 wt
cygb2801a
D
Atrium Area (μm2)
1.5×104
1×104
5×103
0
ns
cygb2 wt
cygb2801a
E
cygb2 wt
cygb2801a
Diastole
Systole
F
Stroke Volume (SV) (μm3)
6×105
4×105
2×105
0
**
cygb2 wt
cygb2801a
G
Diastolic Volume (EDV) (μm3)
8×105
6×105
4×105
2×105
0
**
cygb2 wt
cygb2801a
H
Systolic Volume (ESV) (μm3)
4×105
3×105
2×105
1×105
0
ns
cygb2 wt
cygb2801a
I
cygb2 wt
cygb2801a
J
Ventricle Cell Number
140
120
100
80
ns
cygb2 wt
cygb2801a
K
cygb2 wt
cygb2801a
L
Ventricle Cell Density
150
125
100
75
50
*
cygb2 wt
cygb2801a
M
Ventricle Wall Thickness
2.0
1.5
1.0
0.5
0.0
*
cygb2 wt
cygb2801a

Figure 1

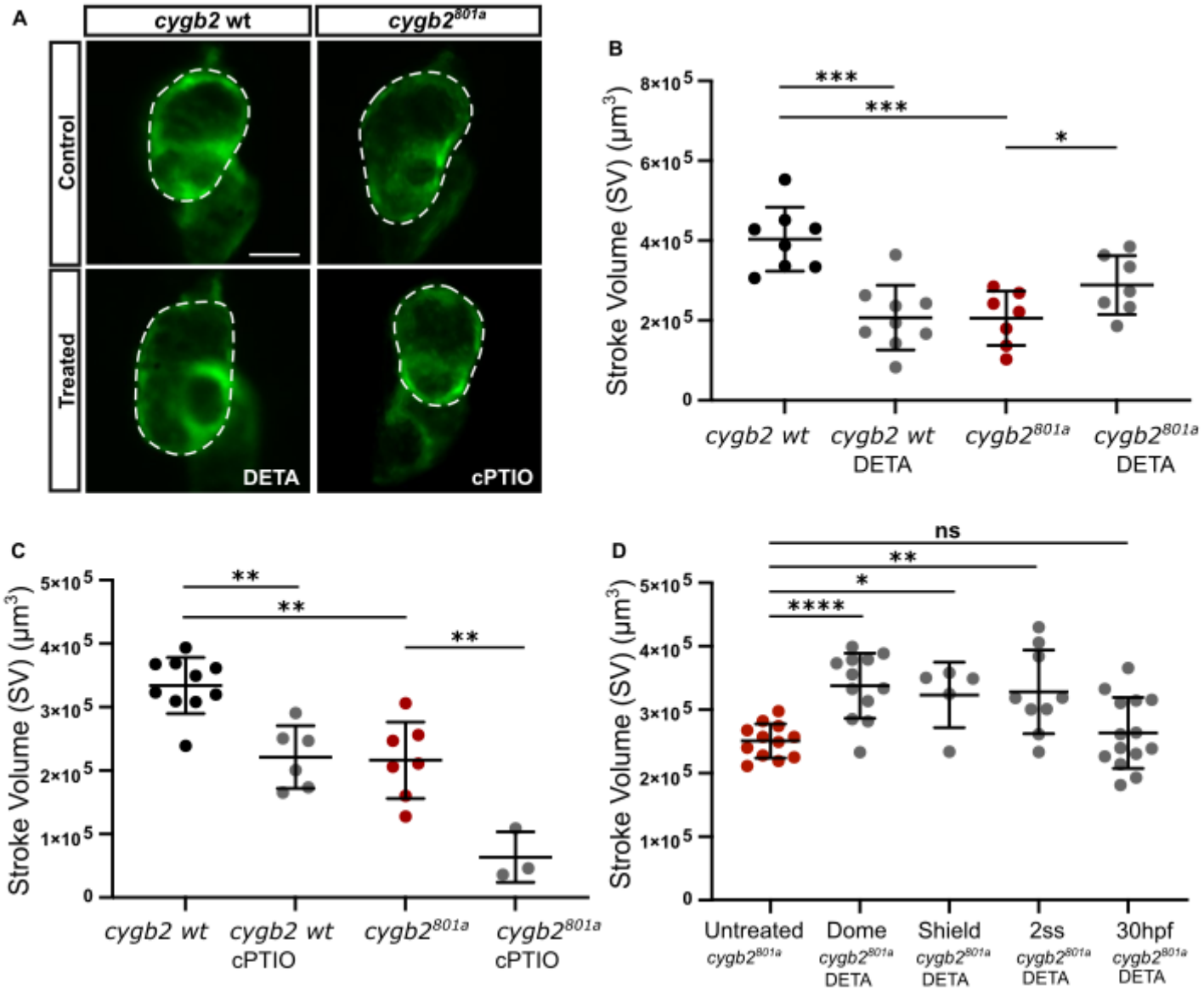
A
cygb2 wt
cygb2801a
Control
Treated
DETA
cPTIO
B
Stroke Volume (SV) (µm3)
8×105
6×105
4×105
2×105
0
***
***
*
cygb2 wt
cygb2 wt DETA
cygb2801a
cygb2801a DETA
C
Stroke Volume (SV) (µm3)
5×105
4×105
3×105
2×105
1×105
0
**
**
**
cygb2 wt
cygb2 wt cPTIO
cygb2801a
cygb2801a cPTIO
D
Stroke Volume (SV) (µm3)
5×105
4×105
3×105
2×105
1×105
0
ns
**
*
****
Untreated cygb2801a
Dome cygb2801a DETA
Shield cygb2801a DETA
2ss cygb2801a DETA
30hpf cygb2801a DETA

Figure 2

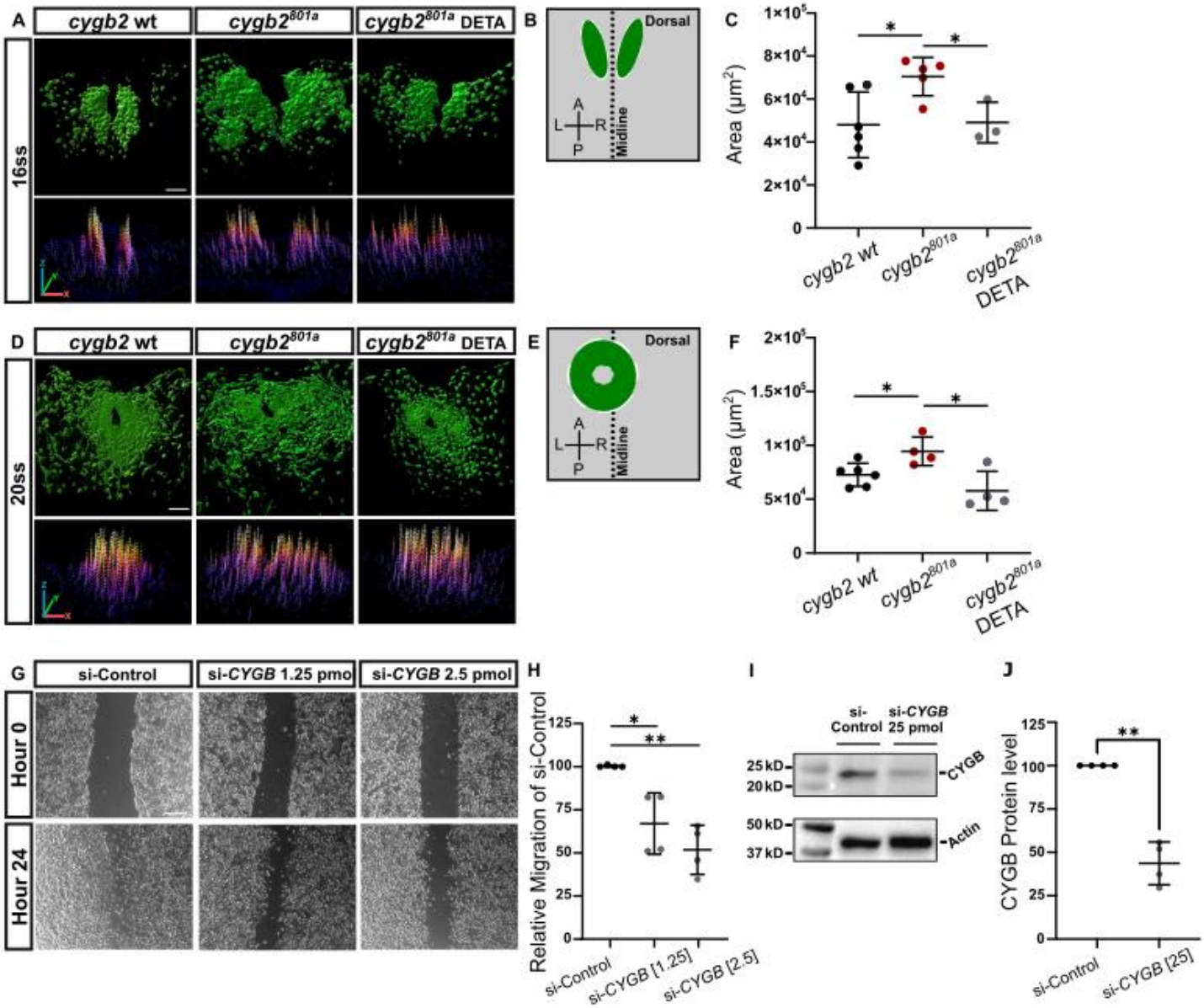
A
cygb2 wt
cygb2801a
cygb2801a DETA
16ss
B
Dorsal
A
L
R
P
Midline
C
Area (μm2)
1×105
8×104
6×104
4×104
2×104
0
*
*
cygb2 wt
cygb2801a
cygb2801a DETA
D
cygb2 wt
cygb2801a
cygb2801a DETA
20ss
E
Dorsal
A
L
R
P
Midline
F
Area (μm2)
2×105
1.5×105
1×105
5×104
0
*
*
cygb2 wt
cygb2801a
cygb2801a DETA
G
si-Control
si-CYGB 1.25 pmol
si-CYGB 2.5 pmol
Hour 0
Hour 24
H
Relative Migration of si-Control
125
100
75
50
25
0
*
**
si-Control
si-CYGB [1.25]
si-CYGB [2.5]
I
si-Control
si-CYGB 25 pmol
25 kD
20 kD
CYGB
50 kD
37 kD
Actin
J
CYGB Protein level
125
100
75
50
25
0
**
si-Control
si-CYGB [25]

Figure 3

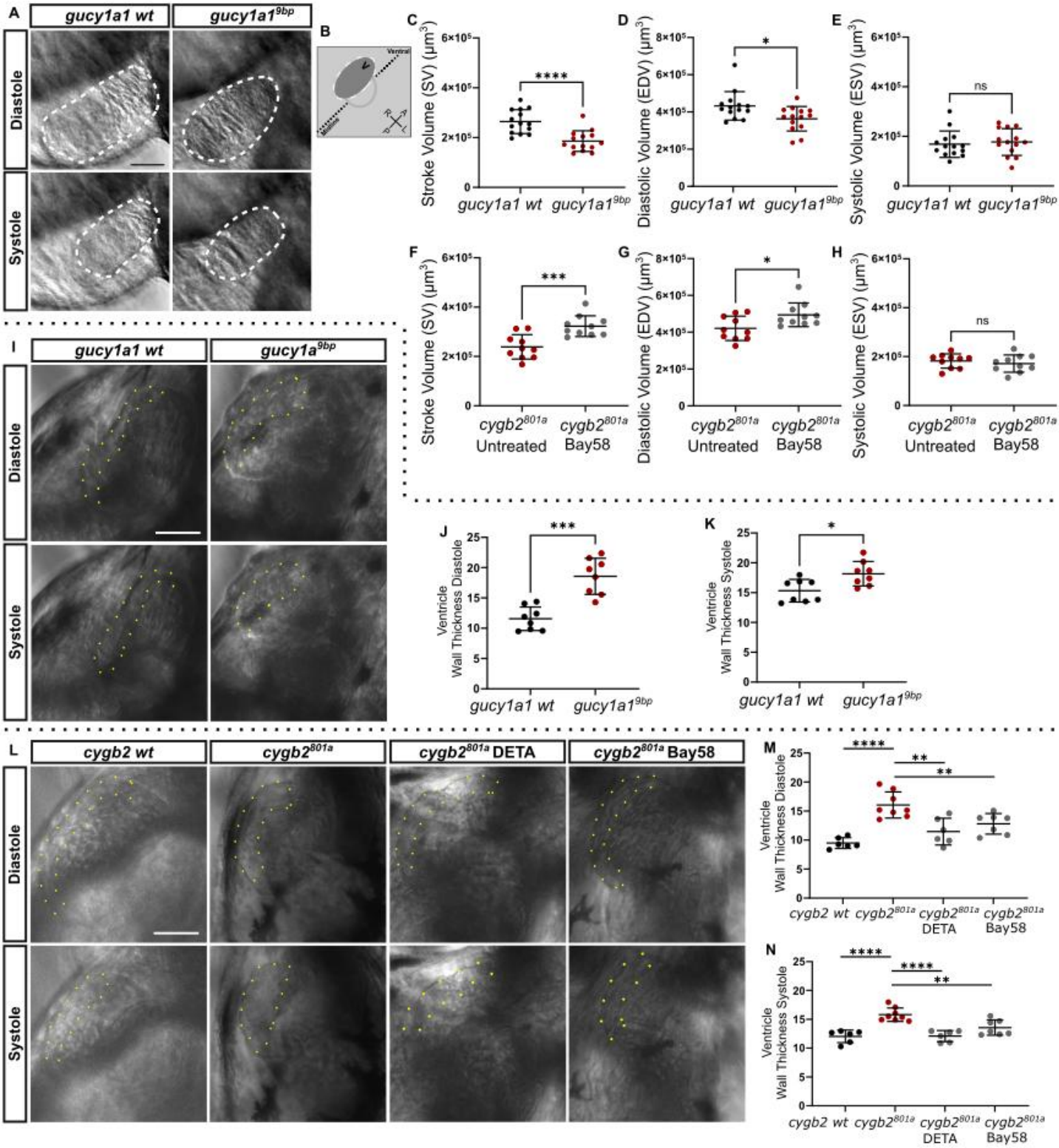
A
gucy1a1 wt
gucy1a1 9bp
Diastole
Systole
B
Ventral
C
Stroke Volume (SV) (µm3)
****
gucy1a1 wt
gucy1a1 9bp
D
Diastolic Volume (EDV) (µm3)
*
E
Systolic Volume (ESV) (µm3)
ns
F
Stroke Volume (SV) (µm3)
***
cygb2 801a Untreated
cygb2 801a Bay58
G
Diastolic Volume (EDV) (µm3)
H
Systolic Volume (ESV) (µm3)
I
gucy1a1 wt
gucy1a 9bp
J
Ventricle Wall Thickness Diastole
K
Ventricle Wall Thickness Systole
L
cygb2 wt
cygb2 801a
cygb2 801a DETA
cygb2 801a Bay58
M
Ventricle Wall Thickness Diastole
**
N
Ventricle Wall Thickness Systole

Figure 4

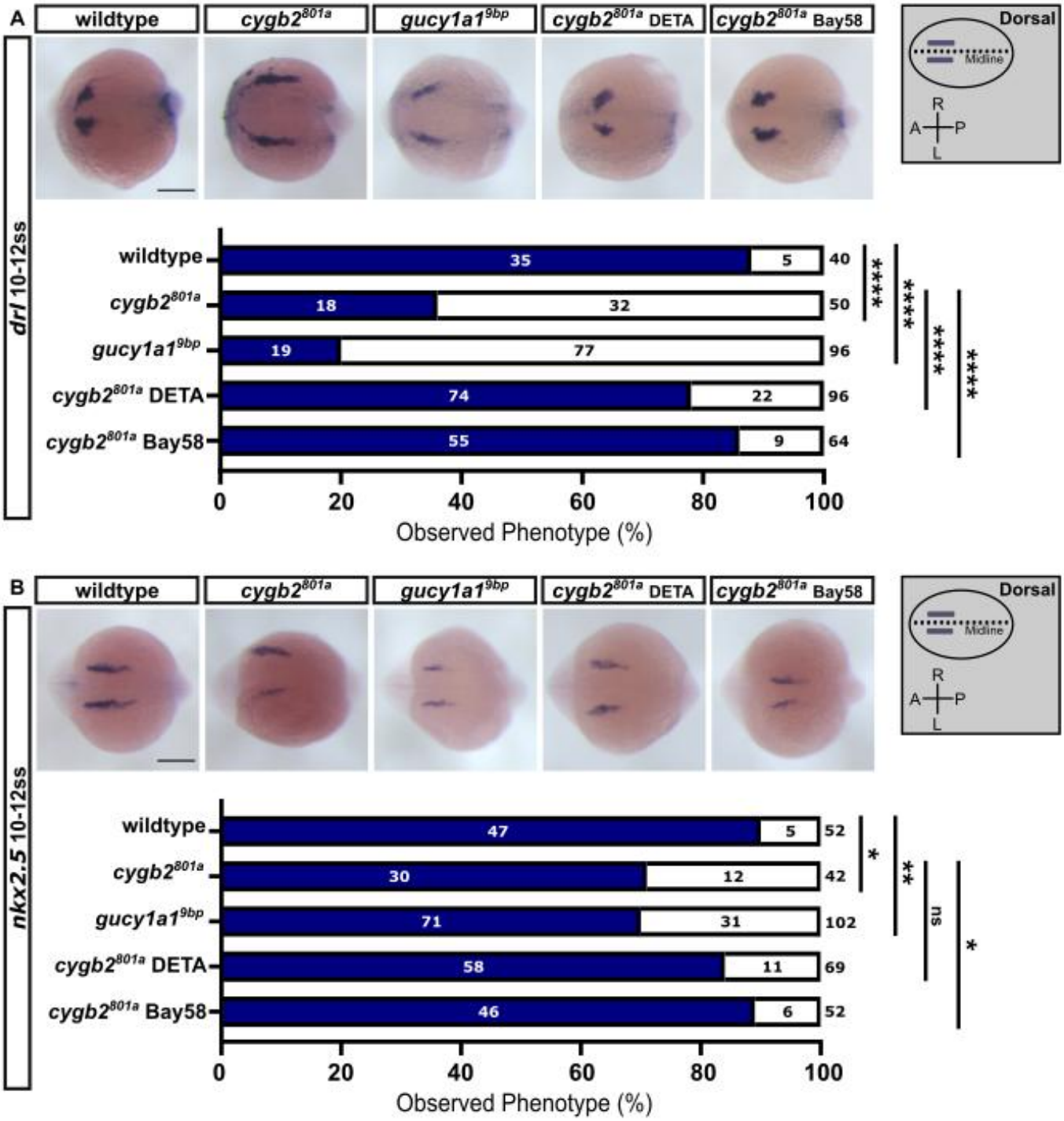
A
wildtype
cygb2801a
gucy1a19bp
cygb2801a DETA
cygb2801a Bay58
Dorsal
Midline
R
A
P
L
drl 10-12ss
wildtype
cygb2801a
gucy1a19bp
cygb2801a DETA
cygb2801a Bay58
35
5
40
18
32
50
19
77
96
74
22
96
55
9
64
****
****
****
****
0
20
40
60
80
100
Observed Phenotype (%)
B
wildtype
cygb2801a
gucy1a19bp
cygb2801a DETA
cygb2801a Bay58
Dorsal
Midline
R
A
P
L
nkx2.5 10-12ss
wildtype
cygb2801a
gucy1a19bp
cygb2801a DETA
cygb2801a Bay58
47
5
52
30
12
42
71
31
102
58
11
69
46
6
52
*
**
ns
*
0
20
40
60
80
100
Observed Phenotype (%)

Figure 5

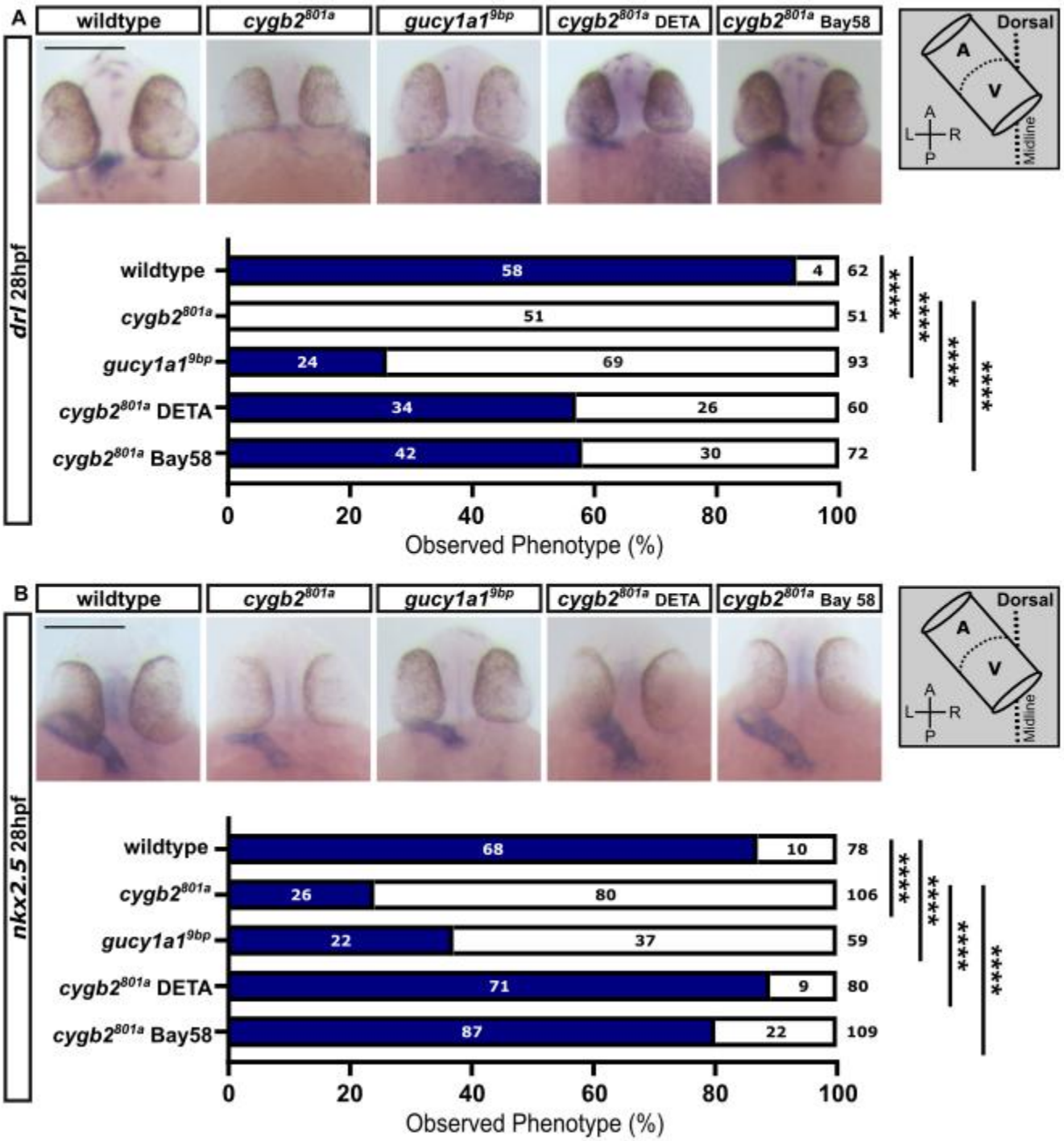
A
wildtype
cygb2801a
gucy1a19bp
cygb2801a DETA
cygb2801a Bay58
Dorsal
A
V
A
L
R
P
Midline
drl 28hpf
wildtype
cygb2801a
gucy1a19bp
cygb2801a DETA
cygb2801a Bay58
58
4
62
51
51
24
69
93
34
26
60
42
30
72
****
****
****
****
0
20
40
60
80
100
Observed Phenotype (%)
B
wildtype
cygb2801a
gucy1a19bp
cygb2801a DETA
cygb2801a Bay 58
Dorsal
A
V
A
L
R
P
Midline
nkx2.5 28hpf
wildtype
cygb2801a
gucy1a19bp
cygb2801a DETA
cygb2801a Bay58
68
10
78
26
80
106
22
37
59
71
9
80
87
22
109
****
****
****
****
0
20
40
60
80
100
Observed Phenotype (%)

Figure 6

760 **Figure Legends**

761

762 **Figure 1. Loss of *cygb2* leads to ventricular hypoplasia and reduced cardiac output. (A)**
763 Representative confocal projections of *cygb2wt*;Tg*(myl7*:EGFP) and *cygb2*^{801a}*;*Tg*(myl7*:EGFP) hearts
764 at 3 days post fertilization (dpf), immuno-labeled for Myh6 (EGFP, green; Myh6, magenta). Scale bar,
765 50µm **(B)** Schematic illustrating heart chamber anatomy and cardiac orientation. A-atrium; V-ventricle;
766 B-bulbus arteriosus **(C,D)** Comparison of ventricle and atrium area. **(E)** Representative frames from
767 fluorescence time-lapse imaging of live *cygb2wt*;Tg*(myl7*:EGFP) and *cygb2*^{801a}*;*Tg*(myl7*:EGFP)
768 embryos 3 dpf showing ventricle volume at diastole and systole, dashed white line demarcates the
769 ventricle (EGFP, green). Scale bar, 50 µm. **(F-H)** Comparison of stroke volume, diastolic volume and
770 systolic volume. **(I)** Representative confocal projections of ventricles at 3 dpf, images are greyscale
771 converted and inverted to highlight cardiomyocyte density. Scale bar, 20µm. **(J)** Comparison of ventricle
772 cell number. **(K)** Representative confocal z-slices at ventricular midpoint. Images were converted to
773 greyscale signal positive area (ventricular myocardium) shown in black. **(L)** Comparison of
774 cardiomyocyte density. **(M)** Comparison of ventricular wall thickness. Sample size (n) corresponds to
775 independent embryos represented by individual data points on plots. Student t-Test; *ns*, not significant;
776 *p<0.05; **p<0.01;***p<0.001

777

778

779 **Figure 2. NO rescues the *cygb2* mutant phenotype, whereas NO scavenging phenocopies the**
780 **mutant. (A)** Representative frames from fluorescent time-lapse imaging of live
781 *cygb2wt*;Tg(*myl7*:EGFP) and *cygb2*^{801a};Tg(*myl7*:EGFP) mutants at 3 days post fertilization (dpf),
782 showing the effect of treatment with a pharmacological NO scavenger (cPTIO) and NO donor (DETA)
783 on diastolic volume (EGFP, green). Scale bar, 50µm. **(B)** Comparison of stroke volume at 3dpf in
784 untreated control and NO donor (DETA) treated, and **(C)** NO scavenger (cPTIO) treated embryos,

785 treatments starting at 2 somite stage (ss). **(D)** Comparison of stroke volumes following chronic
786 treatments starting at different developmental stages (dome, shield, 2ss, and 30hpf). Sample size (n)
787 corresponds to independent embryos represented by individual data points on plots. Student t-Test; *ns*,
788 not significant; *p<0.05; **p<0.01;***p<0.001; ****p<0.0001.
789
790
791 **Fig. 3. *cygb2* mutants show defective cardiac progenitors migration, and CYGB knockdown**
792 **inhibits cell migration in human airway epithelial cell culture. (A,D)** 3D surface rendering and
793 surface plots from *cygb2wt*;Tg(*myl7*:EGFP) and *cygb2*^{801a};Tg(*myl7*:EGFP) showing cardiac progenitors
794 at midline convergence, 16 somite stage (ss), and cardiac disc, 20 ss, renderings and surface plots
795 generated from whole-mount confocal z-series (EGFP, green). NO donor (DETA) treatment starting at
796 2ss. Scale bar, 50µm. (**B,E**) Schematics illustrating cardiac progenitor organization and embryonic
797 orientation. **(C,F)** Effect of chronic DETA treatment on cardiac progenitor organization, represented by
798 EGFP positive area. Treatment starting at 2ss. **(G)** Representative bright-field images of human airway
799 epithelial A549 cultures transfected with a non-targeting (si-Control) and *CYGB* targeting (si-CYGB
800 13.1) siRNAs at 0 and 24 hours post scratch. **(H)** Comparison of percent migration between si-Control
801 and si-*CYGB* at 1.25 pmol and 2.5 pmol. **(I)** Representative images of Western blot bands for CYGB
802 and β-Actin. **(J)** Percent CYGB protein knockdown with si-*CYGB* at 25 pmol relative to si-Control. **(A-**
803 **F)** Sample size (n) corresponds to independent embryos **(G-J)** Sample size (n) corresponds to
804 independent cultures, all represented by individual data points on plots. Student t-Test; *p<0.05;
805 **p<0.01.
806
807
808 **Fig. 4. Ventricle area, ventricular diastolic volume, and stroke volume are reduced, and wall**
809 **thickness is increased in sGC mutants. (A)** Representative frames from DIC time-lapse imaging of

810 live *gucy1a1wt* and *gucy1a1*^{9bp} mutant embryos at 3 days post fertilization (dpf) showing volume at
811 diastole and systole. Scale bar, 50μM. **(B)** Schematic of ventricle position and cardiac orientation. **(C-**
812 **E)** Comparison of stroke volume, diastolic volume, and systolic volume between *gucy1a1wt*, and
813 *gucy1a1*^{9bp}. **(F-H)** Comparisons of stroke volume, diastolic volume, and systolic volume at 3dpf in live
814 untreated and sGC activator (Bay58) treated *cygb2*^{801a};Tg(*myl7*:EGFP) embryos using fluorescent
815 time-lapse imaging, treatments starting at 2 somite stage (ss). **(I,L)** Frames from live DIC time-lapse
816 imaging of *gucy1a1wt*, *gucy1a1*^{9bp} , *cygb2wt* and *cygb2*^{801a} mutants at 3 dpf, depicting ventricle wall
817 thickness at diastole and systole. Scale bar, 50μM. **(L)** NO donor (DETA) and Bay58 treatment starting
818 at 2ss. **(J,K,M,N)** Comparison of wall thickness at diastole and systole. Sample size (n) corresponds to
819 independent embryos represented by individual data points on plots. Student t-Test; *ns*, not significant;
820 *p<0.05; **p<0.01;***p<0.001; ****p<0.0001.
821
822
823 **Fig. 5. Early patterning of the anterior lateral plate mesoderm is disrupted in *cygb2* and *gucy1a1***
824 **mutants and rescued by NO–sGC activation. (A,B)** Representative in situ hybridization images (top)
825 and quantification of *drl* and *nkx2.5* expression patterns (bottom) in embryos at 10-12 somite stage. **(A)**
826 *drl* normal expression pattern is quantified in solid-bars as percentage of embryos with distinct, short,
827 and wide patches of bilateral *drl* expression at anterior edge of anterior lateral plate mesoderm (ALPM).
828 In open-bars, percentage of embryos with elongated incongruous thin lines of bilateral *drl* expression
829 along ALMP. **(B)** *nkx2.5* normal expression pattern is quantified in solid-bars as percentage of embryos
830 with symmetrical, uniform, and distinct bilateral *nkx2.5* expression along ALMP. In open-bars,
831 percentage of embryos with asymmetrical, patchy, or faint bilateral *nkx2.5* expression along ALMP.
832 Number of embryos ranked is listed within and on top of bars. Treatments starting at shield. Scale bar,
833 200μm. On the right, schematic of ALPM anatomy with embryonic orientation. Fishers exact test, ns -
834 not significant ≥ 0.05, * P≤ 0.05, ** P≤ 0.01, *** P≤ 0.001, **** P≤ 0.0001.

835 **Fig. 6. Disrupted specification of endothelial and myocardial lineages persists at 28 hours post**
836 **fertilization and is normalized by restoring NO–sGC signaling. (A,B)** Representative in situ
837 hybridization images (top) and quantification of *drl* and *nkx2.5* expression patterns (bottom) in embryos
838 at 28 hours post fertilization. **(A)** *drl* normal expression pattern is quantified in solid-bars as percentage
839 of embryos with expression in the anterior region of the heart tube. In open-bars, percentage of embryos
840 with complete loss of expression of *drl* in heart tube. **(B)** *nkx2.5* normal expression pattern is quantified
841 in solid-bars as percentage of embryos with distinct clearly defined *nkx2.5* expression along the heart
842 tube full-length. In open-bars, percentage of embryos with reduced or absent *nkx2.5* expression in a
843 shortened heart tube. Number of embryos ranked is listed within and on top of bars. Treatments starting
844 at shield. Scale bar, 200μm. On the right, schematic of the heart tube anatomy with embryonic
845 orientation. Fishers exact test, ns - not significant ≥ 0.05, * P≤ 0.05, ** P≤ 0.01, *** P≤ 0.001, **** P≤
846 0.0001.